Synthesis and photophysical studies of self-assembled multicomponent supramolecular coordination prisms bearing porphyrin faces

Yanhui Shi[a,b,1], Irene Sánchez-Molina[b], Changsheng Cao[a], Timothy R. Cook[b], and Peter J. Stang[b,1]

[a]School of Chemistry and Chemical Engineering and Jiangsu Key Laboratory of Green Synthetic Chemistry for Functional Materials, Jiangsu Normal University, Xuzhou, Jiangsu 221116, People's Republic of China; and [b]Department of Chemistry, University of Utah, Salt Lake City, UT 84112

Contributed by Peter J. Stang, May 14, 2014 (sent for review April 2, 2014)

Multicomponent self-assembly, wherein two unique donor precursors are combined with a single metal acceptor instead of the more common two-component assembly, can be achieved by selecting Lewis-basic sites and metal nodes that select for heteroligated coordination spheres. Platinum(II) ions show a thermodynamic preference for mixed pyridyl/carboxylate coordination environments and are thus suitable for such designs. The use of three or more unique building blocks increases the structural complexity of supramolecules. Herein, we describe the synthesis and characterization of rectangular prismatic supramolecular coordination complexes (SCCs) with two faces occupied by porphyrin molecules, motivated by the search for new multichromophore complexes with promising light-harvesting properties. These prisms are obtained from the self-assembly of a 90° Pt(II) acceptor with a *meso*-substituted tetrapyridylporphyrin (TPyP) and dicarboxylate ligands. The generality of this self-assembly reaction is demonstrated using five dicarboxylate ligands, two based on a rigid central phenyl ring and three alkyl-spaced variants, to form a total of five free-base and five Zn-metallated porphyrin prisms. All 10 SCCs are characterized by ^{31}P and ^{1}H multinuclear NMR spectroscopy and electrospray ionization mass spectrometry, confirming the structure of each self-assembly and the stoichiometry of formation. The photophysical properties of the resulting SCCs were investigated revealing that the absorption and emission properties of the free-base and metallated porphyrin prisms preserve the spectral features associated with free TPyP.

supramolecular chemistry | metallacages

The use of sunlight is ubiquitous as the input for carbon-neutral, renewable energy schemes (1). Every strategy that relies on solar energy conversion, ranging from direct conversion to electricity in photovoltaics (2) to the generation of fuels via electrocatalysis (3), photoanode (4, 5), or photocathode devices (6), or photocatalysis (7) requires that photons be absorbed by a molecule or material as the first step in providing the driving force for subsequent transformation. Natural systems have evolved light-harvesting complexes, comprising multiprotein ensembles embedded with pigment molecules to enhance photon absorption for photosynthesis (8). These pigment-rich sites are arranged such that excitation of a distal chromophore will ultimately result in energy transfer to a reaction center via a series of migration and transfer processes (9). Strategies to replicate natural light-harvesting complexes necessarily demand the organization of multiple chromophores (10), a requirement that makes self-assembly and supramolecular chemistry particularly well suited for such efforts (11–13). As such, a variety of approaches have been applied toward the development of new materials that exhibit broadband absorption and efficient energy transfer (14–16). The subsequent studies of such materials span investigations of the fundamental science behind energy migration and transfer, to practical applications in devices.

Many of these designs incorporate porphyrin-based molecules (17–22), a pigment that is related to the ubiquitous chlorophyll found in natural light-harvesting systems (23). Porphyrins possess characteristic structural and photophysical properties that make them well suited for adaptation into artificial designs, not only for solar energy conversion but also for applications in photodynamic therapy (24–29), enzyme mimics (30–32), catalysis (33–37), and molecular electronic devices (38, 39). In the context of solar energy, many multiporphyrin light-harvesting designs have been developed ranging from organic polymers, metal-organic frameworks, and supramolecular ensembles. Porphyrins are remarkable precursors for incorporation into supramolecular designs due to their established syntheses that facilitate well-defined functionalization, the commercial availability of simple variants, and their ability to accommodate a wide range of metal ions, thus unlocking suites of complexes for a given design (40, 41). The absorption spectra of porphyrin molecules are dominated by so-called Soret bands in the 380- to 500-nm range, accompanied by a set of weaker, but still considerably intense Q bands in the 500- to 700-nm range. Because these bands result in the absorption of visible photons, the attractiveness of porphyrins in solar conversion schemes becomes apparent. Furthermore, the emission wavelengths of a given porphyrin may align with its Q-band absorption, providing the spectral overlap that is required for efficient energy migration.

Although extended structures such as polymers and metal-organic frameworks can organize similar numbers of pigments as are found in natural systems (42–47), their study can be complemented by relatively smaller supramolecules that facilitate characterization and study, preserving attractive properties such as solubility and facile tenability (48, 49). As such, coordination-driven self-assembly has been used to explore porphyrin-based

Significance

Sunlight is an attractive energy source because it is available in amounts that far exceed current and future global demands. Its use, however, requires materials that can efficiently absorb visible wavelength photons. Nature has evolved light-harvesting complexes comprising many pigment molecules to act as antennae, inspiring synthetic designs that similarly organize many chromophores. One method for constructing multiple-pigment ensembles is to use coordination-driven self-assembly. Porphyrin molecules are excellent candidates for both light harvesting and self-assembly, owing to their photophysical properties and rigid framework that allows for directional bonding. Here, we describe the construction of porphyrin prisms using multicomponent self-assembly, wherein 14 total building blocks organize into well-defined metallacages in a single step.

Author contributions: T.R.C. and P.J.S. designed research; Y.S., I.S.-M., C.C., and T.R.C. performed research; Y.S., I.S.-M., T.R.C., and P.J.S. analyzed data; and Y.S., T.R.C., and P.J.S. wrote the paper.

The authors declare no conflict of interest.

[1]To whom correspondence may be addressed. E-mail: stang@chem.utah.edu or yhshi@jsnu.edu.cn.

This article contains supporting information online at www.pnas.org/lookup/suppl/doi:10.1073/pnas.1408905111/-/DCSupplemental.

supramolecular coordination complexes in traditional one- or two-component schemes (50-53).

The recent development of new strategies for multicomponent self-assembly has provided a method to increase the structural complexity of chromophoric supramolecular coordination complexes (SCCs) wherein three or more building blocks can assemble into a single thermodynamically favored product (54, 55). One method to achieve multicomponent assembly is to identify metal nodes and ligands that prefer heteroligated coordination spheres, thus avoiding statistical mixtures of products. For example, when Pt(II) ions are combined with pyridyl and carboxylate-based ligands, mixed Pt-N,O coordination environments are formed exclusively (56). This method has been used recently to construct a variety of 2D and 3D SCCs and also provides the basis for supramolecule-to-supramolecule transformation, wherein a Pt-pyridyl SCC may be mixed in the proper stoichiometry with a Pt-carboxylate SCC to quantitatively furnish a third multicomponent SCC (56). Furthermore, traditional two-component assembly typically requires the use of rigid building blocks so as to maintain the angularity and directionality that determines the structural outcome of a reaction. In contrast, multicomponent approaches also permit the use of structurally ambiguous ligands, provided the remaining building blocks enforce a proper degree of directionality. As such, alkyl-based building blocks may be used in such self-assembly schemes, despite the fact that rotation about the carbon–carbon bonds means that a single orientation of the coordination vectors is not maintained (57).

We report here a unification of many recent themes of coordination-driven self-assembly: the formation of multichromophore complexes as motivated by the need for new light-harvesting materials, multicomponent self assembly using Pt(II) heteroligation, and alkyl-based dicarboxylates in the formation of 3D prisms that demonstrate a hitherto-underexplored class of building blocks for coordination-driven self-assembly. The synthesis and characterization of a suite of 10 prisms is described, thus demonstrating the structural modularity and tunability that is possible through self-assembly approaches. Five prisms are formed containing free-based tetrapyridyl porphyrin, with the remaining five being their Zn-containing analogs. The absorption and emission properties of the SCCs are evaluated and compared with free tetrapyridylporphyrin (TPyP) revealing that, upon incorporation into prisms, the photophysical properties remain largely unchanged. In addition, the solubility of the prisms far exceeds that of the parent TPyP, indicating that coordination-driven self-assembly may be a powerful method to optimize the physiochemical characteristics of new light-harvesting materials.

Results and Discussion

Coordination-driven self-assembly reactions typically require a judicious selection of solvent such that the precursors and any kinetic intermediates remain soluble. Pyridyl/carboxylate multicomponent systems often demand mixed solvent conditions due to the different solubility properties of the precursors. Prism **4a** was first obtained by mixing 90° Pt(II) acceptor **1**, carboxylate ligand **2** with TPyP in a ratio of 8:4:2 (Fig. 1). These precursors were stirred at 70 °C in a mixture of acetone and water (4:1) for 4 h, after which all solvent was removed and the crude product stirred in pure acetone at 70 °C for an additional 4 h (56).

This route was simplified to a single step upon identifying that a three-component solvent mixture of CH_2Cl_2, nitromethane, and acetonitrile (1:1:1) sufficiently solubilized the starting materials and subsequent prisms, allowing quantitative self-assembly to occur. After stirring the building blocks in this mixture for 1 h at 65 °C, **4a–4e** were formed as the sole reaction products based on P{^{1}H} NMR.

The prisms formed using the rigid dicarboxylate building blocks **2a** and **2b** and alkyl-based species **2c–2e** were readily obtained using this method. Attempts to isolate prisms formed with five-carbon or shorter alkyl spacers were unsuccessful, likely due to favorable metallacyclic monomers that may arise for shorter chain lengths. As the dicarboxylate spacer was modified,

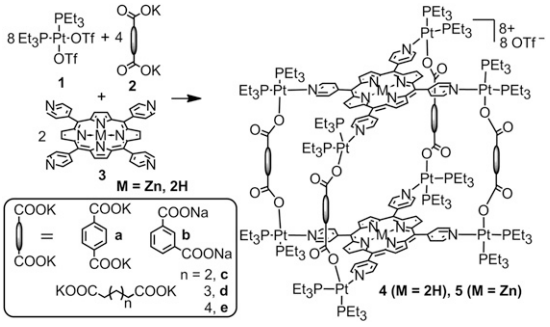

Fig. 1. Self-assembly of tetragonal prisms **4** and **5**.

the solubility of the resulting prisms increased with the trend: isophthalate < terphthalate < C6 < C7 < C8. This is particularly noteworthy in that the solubility of the prisms far exceeded that of free TPyP across most organic solvents, including dimethylformamide, nitromethane, acetone, dichloromethane (DCM), chloroform, methanol, and acetonitrile. Neither the prisms nor free TPyP are appreciably soluble in diethyl ether, hexane, toluene, and ethyl acetate.

All of the described compounds were characterized by multinuclear NMR (^{1}H, ^{31}P), and mass spectrometry (electrospray). The ^{31}P{^{1}H} NMR spectra of porphyrin prisms **4a–4e** show two coupled doublets, at ~2 and 8 ppm (**4a**, 7.68 and 2.72 ppm, $^2J_{p\text{-}p}$ = 21.0 Hz; **4b**, 8.85 and 2.70 ppm, $^2J_{p\text{-}p}$ = 21.1 Hz; **4c**, 7.90 and 1.91 ppm, $^2J_{p\text{-}p}$ = 21.0 Hz; **4d**, 7.73 and 1.67 ppm, $^2J_{p\text{-}p}$ = 21.4 Hz; **4e**, 7.43 and 1.67 ppm, $^2J_{p\text{-}p}$ = 21.4 Hz) of similar intensity with concomitant ^{195}Pt satellites (*SI Appendix*, Figs. S11–S15). The observation of two doublets supports the multicomponent Pt-N,O heteroligated coordination environment in that the symmetry of the two capping phosphine ligands is broken, leading to two unique and coupled resonances. The doublet at ~2 ppm corresponds to the phosphorus nuclei *trans* to the pyridine, whereas the doublet at ~8 ppm is due to the phosphorus nuclei opposite to the carboxylate group. The two doublets of **4a** (5.69 and 0.58 ppm in CCl_2D_2) are upfield-shifted ~3 and 8 ppm, respectively, relative to that for **1** (8.75 ppm in CCl_2D_2) upon coordination. Likewise in the ^{1}H NMR spectra, signals corresponding to the coordinated pyridyl and carboxylate moieties were observed as follows: for **4a**, 9.38 ($H_{\alpha\text{-}Py}$), 8.41 ($H_{\beta\text{-}Py}$), and 8.07 (H_{phenyl}); for **4b**, 9.40 ($H_{\alpha\text{-}Py}$), 8.91 (H_{phenyl}), 8.43 ($H_{\beta\text{-}Py}$), 8.12 (H_{phenyl}), and 7.33 H_{phenyl}); for **4c**, 9.33 ($H_{\alpha\text{-}Py}$), 8.58 ($H_{\beta\text{-}Py}$), and 2.88 ($H_{\alpha\text{-}carboxylic}$); for **4d**, 9.38 ($H_{\alpha\text{-}Py}$), 8.61 ($H_{\beta\text{-}Py}$), and 2.89 ($H_{\alpha\text{-}carboxylic}$); for **4e**, 9.39 ($H_{\alpha\text{-}Py}$), 8.64 ($H_{\beta\text{-}Py}$), and 2.90 ($H_{\alpha\text{-}carboxylic}$). Electrospray ionization (ESI) mass spectral data further support the successful self-assembly of tetragonal prisms **4a–4e** with the expected stoichiometry of 8:4:2. As shown in *SI Appendix*, Figs. S21–S25, peaks corresponding to intact prisms that are charged due to the loss of three triflate anions were observed ($[M\text{-}3OTf]^{3+}$ at m/z = 2,030.12 for **4a**, 2,029.91 for **4b**, 2,003.41 for **4c**, 2,022.12 for **4d**, 2,040.45 for **4e**). All of these peaks are isotopically resolved and agree well with their theoretical distributions.

Obtaining the Zn-metallated analog of **4a–4e** is possible using one of three methods: (*i*) direct metallation of the free-base prisms in a post–self-assembly fashion is possible by stirring a room temperature solution of **4a–4e** with excess $Zn(OAc)_2$ in a 3:1 mixture of chloroform and methanol overnight, in analogy to known procedures (58). This method delivered prisms **5a–5e** in relatively low (<20%) yield. An alternative solvent (CH_2Cl_2) and Zn source [$Zn(OTf)_2$] improved yields to ~50% and facilitated isolation due to the insolubility of the metallated prisms that deposited from solution; (*ii*) the possibility of supramolecular-to-supramolecular transformation was demonstrated by mixing a Pt_6TPyP_3 (**6**) trigonal prism with free dicarboxylate ligands and additional 90° donor, inducing a structural change to prism **4** (56). Similarly, it is possible to transform the Zn analog of **6** into **5a–5e** by introducing the appropriate dicarboxylate ligand and additional

Pt building blocks to match the necessary 8:4:2 stoichiometry. These transformations were carried out in the three-solvent mixture of DCM/$MeNO_2$/MeCN (1:1:1) at 50 °C for 5 h (Fig. 2); and (*iii*) the final route to **5a–5e** involves the pre–self-assembly metallation of TPyP, which can then be used in self-assembly reactions similar to the formation of **4a–4e**, wherein the precursors are simply mixed in an 8:4:2 ratio and stirred at room temperature overnight in DCM/$MeNO_2$/MeCN (1:1:1).

The P{^{1}H} NMR spectra of **5a–5e** were similar to their free-based counterparts as the incorporation of Zn does not have a large effect on the phosphorus resonances. The ^{1}H NMR spectra showed larger changes upon metallation, with the peaks corresponding to the porphyrin protons shifting and a notable disappearance of the NH protons of the free base (located at approximately −3 ppm). In addition, the peaks corresponding to the β-Hs of pyrrole that show up at 9.31 and 7.06 ppm in **4a** shift to 9.15 and 7.13 ppm in **5a** due to the coordination of Zn. Moreover, solutions of the prisms exhibited marked color changes upon metallation, turning from red to purple.

Finally, mass spectrometry experiments confirmed the formation of the metalized porphyrin prisms. Namely, we could observe the signals of $[M\text{-}3OTf]^{3+}$ for all Zn-porphyrin prisms ($[M\text{-}3OTf]^{3+}$ at m/z = 2,072.33 for **5a**, 2,072.32 for **5b**, 2,045.39 for **5c**, 2,064.41 for **5d**, 2,083.41 for **5e**), whose isotopic distributions match their simulated spectra (*SI Appendix*, Figs. S26–S30).

The absorption and emission properties of prisms **4a–4e** and **5a–5e** were investigated to determine whether orienting two porphyrins in a cofacial arrangement would have an effect on their photophysics and to what extent this effect could be tuned by altering the dicarboxylate (rigidity, separation distance) or metal.

Prisms **4a–4e** were investigated in both CH_2Cl_2 and acetone, whereas **5a–5e** were investigated in DMSO and acetone due to a lack of solubility of TPyP and Zn-TPyP, making it difficult to find a single solvent to compare all prisms and free precursors (Table 1 and Fig. 3). The absorption and emission bands observed for **4a–4e** were similar to those found for free TPyP.

The prisms displayed the characteristic Soret band in the 420- to 423-nm range along with four Q bands located at 514–515 nm (Q4), 548–554 nm (Q3), 589–592 nm (Q2), and 641–644 nm (Q1). The Q and Soret bands correspond respectively to the first and second excited singlet states of the porphyrin (59, 60). Compared with the bands of TPyP, the Soret bands of **4a–4e** showed ∼4- to 7-nm red shifts. In addition, a 2- to 4-nm red shift of the Q bands in complexes **4a–4e** was observed as well.

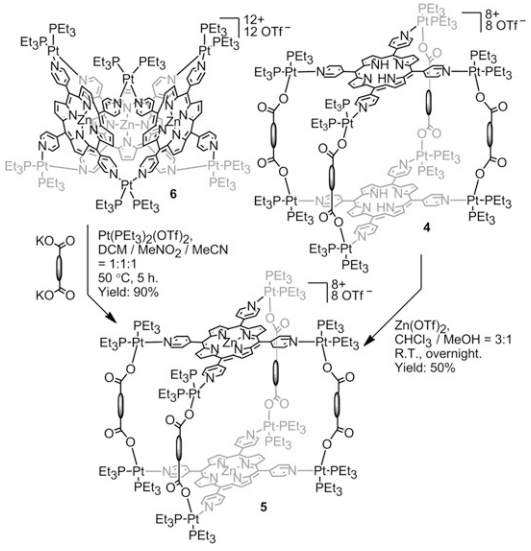

Fig. 2. Metallation of porphyrin prisms with Zn(II).

When the alkyl-chain length is varied between **4c–4e**, relatively minor changes to intensity and wavelength are observed between the absorption spectra of the prisms. Modest 1- to 2-nm red shifts occur relative to the Soret bands in **4a** and **4b**. Likewise, the molar absorption coefficients of the Soret band in **4c–4d** are very similar (∼642,000 $cm^{-1}{\cdot}M^{-1}$), and only slightly lower than those in **4a–4b** (661,000 $cm^{-1}{\cdot}M^{-1}$ for **4a** and 655,000 $cm^{-1}{\cdot}M^{-1}$ for **4b**). These intensities are significantly greater than the Soret band in free TPyP, as expected due to the presence of two porphyrin units per prism. Although the intensity is larger for the prisms, some coupling between the porphyrins is evidenced by the fact that the Soret band of free TPyP is greater than half that of **4a–4e** (359,000 $cm^{-1}{\cdot}M^{-1}$ for TPyP) in CH_2Cl_2.

The absorption spectra of **5a–5e** collected in DMSO showed typical metallaporphyrin behavior (Fig. 3, *Upper Right*), displaying a characteristic Soret band and three less intensive Q bands located at 518–522 nm (Q4), 556–559 nm (Q3), and 594–599 nm (Q2). The Soret bands of **5a** and **5c–5e** are unchanged compared with that of Zn-TPyP, and only a 1-nm red shift was observed in **5b**. However, some of the Q bands in **5a–5e** appear bathochromically shifted, for example, 1- to 4-nm and 2-nm shifts of bands Q4 and Q3, respectively, were found in **5b–5e**. Similar to what was observed for **4a–4e**, the absorptivity per Zn-porphyrin unit is lower for the prisms than for free Zn-TPyP. Likewise, variations of the dicarboxylate ligand cause minor changes to the intensity and wavelength of the absorption features as well; however, there is no consistent trend between the systems.

In addition, the absorption spectra of all assembly complexes **4a–4e** and **5a–5e** were investigated in acetone to investigate the effect of the coordinated metal (Table 1). A slight bathochromic shift (4–6 nm) of the Soret band responsible for the purple color of all assembly complexes **5** is observed. The Q1 band totally disappeared in **5**, and the intensity of the Q4 band decreased significantly due to a more symmetrical situation in Zn coordinated complex **5** than in complexes **4** with free-base porphyrin. The relative intensities of these Q bands (Q3 > Q4) shows that the zinc metal forms a stable square-planar complex with the porphyrin in complex **5**. The molar absorption coefficient of the Soret band in **5**, at 6–8 × 10^5 $cm^{-1}{\cdot}M^{-1}$, is comparable to that in **4**.

The emission spectra of prisms **4a–4e** and TPyP were collected in CH_2Cl_2 via irradiation of each compound's Soret band and Q4 band (Fig. 3, *Lower Left*). Prisms **4a–4e** show typical porphyrin-based fluorescence spectra characterized by two bands at ∼645 nm [$Q_{(0,0)}$] with high intensity and ∼708 nm [$Q_{(0,1)}$] with low intensity, corresponding to emission from the S_1 singlet state of the porphyrin. The emission spectrum is independent of the excitation wavelength, due to the $S_2 \rightarrow S_1$ internal conversion. Relatively minor shifts (<6 nm) of the emission bands of **4a–4e** were observed with respect to free TPyP. For example, a 2- to 4-nm red shift of the $Q_{(0,0)}$ band was observed in **4a** and **4c–4e**, whereas a 2-nm blue shift was observed in **4b**. The wavelength of the $Q_{(0,1)}$ band in **4d–4e** was unchanged compared with that in the free base porphyrin, whereas 5 nm of blue shift was observed in **4a**. It is interesting that the emission profile in **4a–4b** changes compared with **4c–4e**, in particular in the relative intensities of the $Q_{(0,0)}$ and $Q_{(0,1)}$ bands. It is know that the intensity and spectral position of the $Q_{(0,0)}$ band is very sensitive to the peripheral substituents and changes of the $Q_{(0,0)}$ band in different solvents of different porphyrins have been reported (61). Stokes shifts of 3,903–4,047 cm^{-1} were observed in **4a–4e** with quantum yields between 0.04% and 0.06% (**4a**: 0.051%; **4b**: 0.037%; **4c**: 0.056%; **4d**: 0.048%; **4e**: 0.061%) when measured against rhodamine 6G. Although there is no clear trend for the quantum yields in prism **4**, it is worth noting that the prism **4b** with the shortest porphyrin–porphyrin distance displays the lowest quantum yield, and **4e** with the longest distance display the highest quantum yield. The variation of quantum yields probably results from a combination of effects, including the porphyrin–porphyrin distance and overall rigidity of the structure. Rigidifying the structure with phenyl ligands may reduce nonradiative vibrational relaxation pathways, but may at the same time introduce

Table 1. Absorption data of compounds 4a–4e, 5a–5e, and porphyrins in different solvents

Compound	λ_{max}, nm ($\varepsilon \times 10^4$, $cm^{-1}\cdot M^{-1}$), CH_2Cl_2	λ_{emiss}, nm, CH_2Cl_2	λ_{max}, nm ($\varepsilon \times 10^4$, $cm^{-1}\cdot M^{-1}$), DMSO	λ_{emiss}, nm, DMSO	λ_{max}, nm ($\varepsilon \times 10^4$, $cm^{-1}\cdot M^{-1}$), acetone	λ_{emiss}, nm, acetone
4a	420 (66.1), 514 (4.91), 554 (1.82), 590 (2.24), 642 (1.19)	647, 703	—	—	416 (75.6), 510 (4.91), 542 (1.73), 586 (1.82), 640 (0.85)	643, 704
4b	421 (65.5), 514 (4.66), 552 (1.99), 591 (2.07), 641 (1.08)	643, 707	—	—	414 (66.0), 509 (4.08), 542 (1.60), 586 (1.63), 640 (0.85)	642, 706
4c	422 (64.2), 514 (6.52), 552 (5.81), 595 (4.06), 643 (2.29)	649, 707	—	—	414 (67.5), 510 (3.97), 542 (1.69), 586 (1.53), 639 (0.77)	643, 705
4d	422 (64.2), 515 (5.36), 548 (3.18), 592 (2.69), 644 (1.77)	647, 708	—	—	416 (69.8), 510 (4.11), 542 (1.88), 586 (1.59), 639 (0.78)	644, 707
4e	423 (64.1), 514 (4.25), 548 (2.30), 589 (1.87), 644 (1.10)	647, 708	—	—	414 (65.6), 510 (4.11), 542 (2.01), 586 (1.69), 642 (0.96)	644, 705
4-TPyP	416 (35.9), 512 (2.00), 546 (0.73), 586 (0.77), 640 (0.39)	645, 708	—	—		
5a	—	—	426 (99.6), 518 (5.43), 556 (5.46), 594 (3.76)	601, 652	420 (76.3), 518 (2.82), 554 (3.76), 586 (2.15)	599, 647
5b	—	—	427 (81.0), 519 (3.35), 559 (6.06), 595 (3.26)	603, 652	420 (79.9), 517 (1.36), 554 (4.13), 591 (1.50)	599, 648
5c	—	—	426 (86.7), 522 (1.48), 559 (4.12), 595 (1.73)	603, 652	422 (71.1), 516 (1.20), 554 (3.81), 592 (1.28)	600, 649
5d	—	—	426 (94.0), 521 (1.80), 559 (4.53), 599 (2.01)	602, 653	421 (69.1), 516 (1.13), 554 (3.67), 592 (1.26)	602, 650
5e	—	—	426 (102), 521 (1.97), 559 (5.11), 599 (2.41)	602, 654	420 (63.2), 516 (1.14), 554 (3.44), 592 (1.28)	602, 650
Zn-TPyP	—	—	426 (51.8), 518 (0.81), 557 (2.31), 596 (1.02)	602, 653		

electronic communication between porphyrin units and routes for nonradiative decay. As the prism is expanded, the porphyrin units become more isolated, better resembling the free TPyP that displays the highest quantum yield (0.096%). The decrease in quantum yield of the prisms relative to free TPyP is attributed in part to the Pt heavy atom effect. Heavy atoms enhance spin-orbit coupling of a formally spin-forbidden deactivation process of the singlet state of the porphyrin (62). Although Pt is a promising metal from a structural standpoint, future designs may display improved photophysical properties by incorporating alternative metals so as to minimize spin-orbit coupling.

The emission spectra of complexes **5a–5e** and Zn-TPyP were collected in DMSO via irradiation of the Soret band and Q4 bands (Fig. 3). The fluorescence spectra of prisms **5a–5e** are similar to that of Zn-TPyP, with two bands at ~602 and ~653 nm. Even smaller shifts were observed for **5a–5e** relative to Zn-TPyP versus that of **4a–4e** and TPyP, with <1-nm differences between the emission bands of the Zn prisms and Zn-TPyP. Comparing the emission spectra of complexes **4a–4e** with **5a–5e** in acetone (*SI Appendix*, Figs. S31–S32) shows that insertion of zinc changed the general shape of the emission spectra and led to a blue shift of the emission bands (~42 nm) compared with those of the metal-free porphyrins assemblies.

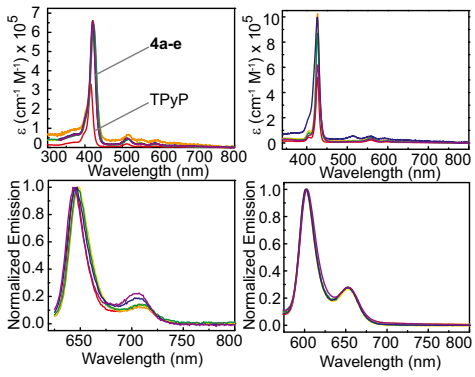

Fig. 3. Absorption (*Upper Left*) and emission (*Lower Left*) profiles for TpyP (red), **4a** (blue), **4b** (purple), **4c** (orange), **4d** (yellow), and **4e** (green) in DCM. Absorption (*Upper Right*) and emission (*Lower Right*) profiles for Zn-TpyP (red), **5a** (blue), **5b** (purple), **5c** (green), **5d** (yellow), and **5e** (orange) in DMSO.

The fluorescence quantum yields of **5a–5e** are relatively invariant, with the phenyl-based prisms slightly higher than their alkyl counterparts ($\Phi = 0.17\%$ for **5a**, $\Phi = 0.18\%$ for **5b**, $\Phi = 0.13\%$ for **5c**, $\Phi = 0.11\%$ for **5d**, and $\Phi = 0.10\%$ for **5e**). The quantum yields of the prisms are much lower than that of free Zn porphyrin ($\Phi = 0.59\%$ for Zn-TPyP), attributed to the heavy metal effect of Pt, as was the case for **4** versus TPyP. Similarly to what is observed for TPyP and Zn-TPyP, prisms **5a–5e** show higher quantum yields than **4a–4e**. The shorter Zn prisms have marginally higher quantum yields than the longer alkyl spaced variants, suggesting that, for the metallated prisms, rigidifying the structure is more important than electronically isolating the porphyrin subunits.

Conclusion

Organic chromophore molecules may be readily incorporated into coordination-driven self-assembly schemes using the directional bonding approach in efforts to mimic natural light-harvesting systems. Recent advances in multicomponent self-assembly motivate the mixed ligand systems reported here, wherein tetrapyridyl porphyrins are combined with carboxylate donors and Pt-based acceptors. The thermodynamic preference for heteroligation of Pt(II) enables the formation of a suite of prismatic complexes using dicarboxylate donors of differing lengths and rigidities. We have used this approach to generate 10 such prisms, unifying the themes of coordination-driven self-assembly, multicomponent architectures, and alkyl-based building blocks. The tunability of these prisms is further demonstrated through the formation of both free-base and Zn-metallated analogs. Photophysical investigations reveal that both types of prisms maintain the attractive properties of their parent porphyrin building blocks, with minor intensity and wavelength changes

occurring upon self-assembly. Although the absorption and emission behaviors are maintained, the solubilities of the prisms is enhanced relative to the free porphyrins, indicating that such self-assembly schemes are promising for optimizing the properties of new light-harvesting materials.

Materials and Methods

cis-Pt(PEt_3)$_2$(OTf)$_2$ (**1**) was prepared according to literature procedures (23). Dicarboxylic ligand **2** was prepared by neutralization of the corresponding acid with 2 eq of NaOH or KOH. All other compounds were used as bought from Sigma-Aldrich, whereas deuterated solvents were purchased from Cambridge Isotope Laboratory. ^{1}H and ^{31}P{^{1}H} spectra were recorded on a Varian 300 spectrometer and the mass spectra were recorded on a Micromass LCT Premier XE TOF mass spectrometer using ESI and analyzed using the MassLynx software suite. The ESI-MS samples were dissolved in acetone. All ^{31}P{^{1}H} spectra were referenced using a 10% (wt/vol) H_3PO_4 aqueous solution.

General Procedure for Multicompound Self-Assembly 4 and 5. To a 2-dram vial, *cis*-Pt(PEt_3)$_2$(OTf)$_2$ (**1**) (4 eq), dicarboxylate ligand (**2**) (2 eq), and 5,10,15,20-tetrakis-(4-pyridyl)-21,23H-porphyrin (**3**) (1 eq) were placed, and the mixed solvent of MeCN/$MeNO_2$/CH_2Cl_2 (1:1:1) was added. The mixture was stirred at 60 °C for overnight, and the resulting mixture was cooled and filtered. The multicomponent self-assembly products were isolated via precipitation by additions of diethyl ether into the concentrated filtrate.

Synthesis and Characterization of 4a. Reaction scale was as follows: *cis*-Pt(PEt_3)$_2$(OTf)$_2$ (**1**) (4.11 mg, 5.64 mmol), potassium *tert*-phthalate (0.77 mg, 3.67 mmol), **3** (0.88 mg, 1.38 mmol), and 1 mL of solvent. Compound **4a** was obtained as reddish-brown solid (4.2 mg, 93%). ^{1}H NMR (300 MHz, acetone-d_6): δ = 9.38 (d, 16H, *J* = 4.1 Hz, α-Py-H), 9.31 (s, 8H, pyrrole-H), 8.41 (d, 16H, *J* = 4.1 Hz, β-Py-H), 8.07 (s, 16H, phenyl-H), 7.06 (s, 8H, pyrrole-H), 2.41–2.19 (m, 96H, P-C*H*$_2$-CH$_3$), 1.57–1.40 (m, 144H, P-CH$_2$-C*H*$_3$), −3.30 (br, 4H, N*H*). ^{31}P{^{1}H}NMR (acetone-d_6, 121.4 MHz): δ = 7.68 (d, $^2J_{p\text{-}p}$ = 21.0 Hz, ^{195}Pt satellites, $^1J_{pt\text{-}p}$ = 3,281 Hz), 2.72 ($^2J_{p\text{-}p}$ = 21.0 Hz, ^{195}Pt satellites, $^1J_{pt\text{-}p}$ = 3,682 Hz). ESI-MS ($C_{213}H_{308}F_{15}N_{16}O_{31}P_{16}Pt_8S_5$) *m/z*: [M-3OTf]$^{3+}$ 2,030.12.

Synthesis and Characterization of 4b. Reaction scale was as follows: *cis*-Pt(PEt_3)$_2$(OTf)$_2$ (**1**) (7.88 mg, 10.81 mmol), sodium *iso*-phthalate (1.14 mg, 5.44 mmol), **3** (1.96 mg, 2.72 mmol), and 2 mL of solvent. Compound **4b** was obtained as reddish-brown solid (8.2 mg, 94%). ^{1}H NMR (300 MHz, acetone-d_6): δ = 9.40 (s, 16H, α-Py-H), 9.34 (s, 8H, pyrrole-H), 8.91 (s, 4H, Ph-H), 8.43 (s, 16H, β-Py-H), 8.12 (d, 8H, *J* = 6.7 Hz, phenyl-H), 7.74 (s, 8H, pyrrole-H), 7.33 (t, 4H, *J* = 6.5 Hz, phenyl-H), 2.35–2.21 (m, 96H, P-C*H*$_2$-CH$_3$), 1.48 (m, 144H, P-CH$_2$-C*H*$_3$), −3.29 (br, 4H, N*H*). ^{31}P{^{1}H}NMR (acetone-d_6, 121.4 MHz): δ = 8.85 (d, $^2J_{p\text{-}p}$ = 21.1 Hz, ^{195}Pt satellites, $^1J_{pt\text{-}p}$ = 3,258 Hz), 2.70 ($^2J_{p\text{-}p}$ = 21.1 Hz, ^{195}Pt satellites, $^1J_{pt\text{-}p}$ = 3,440 Hz). ESI-MS ($C_{213}H_{308}F_{15}N_{16}O_{31}P_{16}Pt_8S_5$) *m/z*: [M-3OTf]$^{3+}$ 2,029.91.

Synthesis and Characterization of 4c. Reaction scale was as follows: *cis*-Pt(PEt_3)$_2$(OTf)$_2$ (**1**) (9.22 mg, 12.65 mmol), potassium hexanedioate (1.30 mg, 6.19 mmol), **3** (2.01 mg, 3.16 mmol), and 2 mL of solvent. Compound **4c** was obtained as reddish-brown solid (9.2 mg, 90%). ^{1}H NMR (300 MHz, acetone-d_6): δ = 9.38 (s, 8H, pyrrole-H), 9.33 (m, 16H, α-Py-H), 8.58 (d, 16H, *J* = 5.4 Hz, β-Py-H), 8.35 (s, 8H, pyrrole-H), 2.88 (br, 16H, CO_2CH_2), 2.30–2.10 (m, 96H, P-C*H*$_2$-CH$_3$), 1.64 (s, 16H, C*H*$_2$), 1.52–1.36 (m, 144H, P-CH$_2$-C*H*$_3$), −3.01 (br, 4H, N*H*). ^{31}P{^{1}H}NMR (acetone-d_6, 121.4 MHz): δ = 7.90 (d, $^2J_{p\text{-}p}$ = 21.0 Hz, ^{195}Pt satellites, $^1J_{pt\text{-}p}$ = 3,288 Hz), 1.91 ($^2J_{p\text{-}p}$ = 21.0 Hz, ^{195}Pt satellites, $^1J_{pt\text{-}p}$ = 3,392 Hz). ESI-MS ($C_{205}H_{324}F_{15}N_{16}O_{31}P_{16}Pt_8S_5$) *m/z*: [M-3OTf]$^{3+}$ 2,003.41.

Synthesis and Characterization of 4d. Reaction scale was as follows: *cis*-Pt(PEt_3)$_2$(OTf)$_2$ (**1**) (8.37 mg, 11.98 mmol), potassium heptanedioate (1.29 mg, 6.09 mmol), **3** (1.95 mg, 3.06 mmol), and 2 mL of solvent. Compound **4d** was obtained as reddish-brown solid (8.8 mg, 91%). ^{1}H NMR (300 MHz, acetone-d_6): δ = 9.38 (m, 16H, α-Py-H), 9.32 (s, 8H, pyrrole-H), 8.61 (m, 24H, β-Py-H, pyrrole-H), 2.89 (br, 16H, CO_2CH_2), 2.29–2.13 (m, 96H, P-C*H*$_2$-CH$_3$), 1.69 (m, 24H, C*H*$_2$), 1.51–1.36 (m, 144H, P-CH$_2$-C*H*$_3$), −2.98 (br, 4H, N*H*). ^{31}P{^{1}H}NMR (acetone-d_6, 121.4 MHz): δ = 7.73 (d, $^2J_{p\text{-}p}$ = 21.4 Hz, ^{195}Pt satellites, $^1J_{pt\text{-}p}$ = 3,237 Hz), 1.67 ($^2J_{p\text{-}p}$ = 21.4 Hz, ^{195}Pt satellites, $^1J_{pt\text{-}p}$ = 3,360 Hz). ESI-MS ($C_{209}H_{332}F_{15}N_{16}O_{31}P_{16}Pt_8S_5$) *m/z*: [M-3OTf]$^{3+}$ 2,022.12.

Synthesis and Characterization of 4e. Reaction scale was as follows: *cis*-Pt(PEt_3)$_2$(OTf)$_2$ (**1**) (8.75 mg, 12.02 mmol), potassium octanedioate (1.31 mg, 6.11 mmol), **3** (1.94 mg, 3.06 mmol), and 2 mL of solvent. Compound **4e** was obtained as reddish-brown solid (9.0 mg, 91%). ^{1}H NMR (300 MHz, acetone-d_6): δ = 9.39 (br, 16H, α-Py-H), 9.28 (s, 8H, pyrrole-H), 8.73 (s, 8H, pyrrole-H,), 8.64 (s, 16H, β-Py-H), 2.90 (m, 16H, CO_2CH_2), 2.30–2.12 (m, 96H, P-C*H*$_2$-CH$_3$), 1.61 (m, 16H, C*H*$_2$), 1.50–1.36 (m, 144H, P-CH$_2$-C*H*$_3$), 1.22 (m, 16H, CH$_2$), −2.97 (br, 4H, N*H*). ^{31}P{^{1}H}NMR (acetone-d_6, 121.4 MHz): δ = 7.43 (d, $^2J_{p\text{-}p}$ = 21.4 Hz, ^{195}Pt satellites, $^1J_{pt\text{-}p}$ = 3,282 Hz), 1.67 ($^2J_{p\text{-}p}$ = 21.4 Hz, ^{195}Pt satellites, $^1J_{pt\text{-}p}$ = 3,373 Hz). ESI-MS ($C_{213}H_{340}F_{15}N_{16}O_{31}P_{16}Pt_8S_5$) *m/z*: [M-3OTf]$^{3+}$ 2,040.45.

Synthesis and Characterization of 5a. Reaction scale was as follows: *cis*-Pt(PEt_3)$_2$(OTf)$_2$ (**1**) (5.73 mg, 7.85 mmol), potassium *tert*-phthalate (0.95 mg, 3.93 mmol), Zn-**3** (1.34 mg, 1.96 mmol), and 2 mL of solvent. Compound **5a** was obtained as purple solid (6.2 mg, 95%). ^{1}H NMR (300 MHz, acetone-d_6): δ = 9.36 (m, 16H, α-Py-H), 9.15 (s, 8H, pyrrole-H), 8.35 (m, 16H, β-Py-H), 8.09 (s, 16H, phenyl-H), 7.13 (s, 8H, pyrrole-H), 2.41–2.17 (m, 96H, P-C*H*$_2$-CH$_3$), 1.58–1.40 (m, 144H, P-CH$_2$-C*H*$_3$). ^{31}P{^{1}H}NMR (acetone-d_6, 121.4 MHz): δ = 7.56 (d, $^2J_{p\text{-}p}$ = 20.8 Hz, ^{195}Pt satellites, $^1J_{pt\text{-}p}$ = 3,245 Hz), 2.62 ($^2J_{p\text{-}p}$ = 21.4 Hz, ^{195}Pt satellites, $^1J_{pt\text{-}p}$ = 3,463 Hz). ESI-MS ($C_{216}H_{304}F_{24}N_{16}O_{40}P_{16}Pt_8S_8Zn_2$) *m/z*: [M-3OTf]$^{3+}$ 2,072.33, [M-4OTf]$^{4+}$ 1,516.35.

Synthesis and Characterization of 5b. Reaction scale was as follows: *cis*-Pt(PEt_3)$_2$(OTf)$_2$ (**1**) (4.03 mg, 5.52 mmol), sodium *iso*-phthalate (0.60 mg, 2.86 mmol), **3** (0.94 mg, 1.38 mmol), and 1 mL of solvent. Compound **5b** was obtained as purple solid (4.1 mg, 90%). ^{1}H NMR (300 MHz, acetone-d_6): δ = 9.36 (m, 16H, α-Py-H), 9.21 (s, 8H, pyrrole-H), 8.96 (s, 4H, Ph-H), 8.36 (d, 16H, *J* = 5.7 Hz, β-Py-H), 8.12 (d, 8H, *J* = 6.7 Hz, phenyl-H), 7.76 (s, 8H, pyrrole-H), 7.32 (t, 4H, *J* = 7.5 Hz, phenyl-H), 2.39–2.12 (m, 96H, P-C*H*$_2$-CH$_3$), 1.57–1.41 (m, 144H, P-CH$_2$-C*H*$_3$). ^{31}P{^{1}H}NMR (acetone-d_6, 121.4 MHz): δ = 8.77 (d, $^2J_{p\text{-}p}$ = 21.4 Hz, ^{195}Pt satellites, $^1J_{pt\text{-}p}$ = 3,264 Hz), 2.65 ($^2J_{p\text{-}p}$ = 20.8 Hz, ^{195}Pt satellites, $^1J_{pt\text{-}p}$ = 3,440 Hz). ESI-MS ($C_{216}H_{304}F_{24}N_{16}O_{40}P_{16}Pt_8S_8Zn_2$) *m/z*: [M-3OTf]$^{3+}$ 2,072.32, [M-4OTf]$^{4+}$ 1,516.85.

Synthesis and Characterization of 5c. Reaction scale was as follows: *cis*-Pt(PEt_3)$_2$(OTf)$_2$ (**1**) (4.28 mg, 5.87 mmol), potassium hexanedioate (0.65 mg, 2.94 mmol), Zn-**3** (1.00 mg, 1.47 mmol), and 1 mL of solvent. Compound **5c** was obtained as purple solid (4.4 mg, 90%). ^{1}H NMR (300 MHz, acetone-d_6): δ = 9.26 (m, 16H, α-Py-H), 9.19 (s, 8H, pyrrole-H), 8.48 (d, 16H, *J* = 5.4 Hz, β-Py-H), 8.37 (s, 8H, pyrrole-H), 2.80 (br, 16H, CO_2CH_2), 2.29–2.15 (m, 96H, P-C*H*$_2$-CH$_3$), 1.63 (s, 16H, C*H*$_2$), 1.50–1.35 (m, 144H, P-CH$_2$-C*H*$_3$). ^{31}P{^{1}H}NMR (acetone-d_6, 121.4 MHz): δ = 7.82 (d, $^2J_{p\text{-}p}$ = 20.8 Hz, ^{195}Pt satellites, $^1J_{pt\text{-}p}$ = 3,283 Hz), 1.88 ($^2J_{p\text{-}p}$ = 20.8 Hz, ^{195}Pt satellites, $^1J_{pt\text{-}p}$ = 3,368 Hz). ESI-MS ($C_{208}H_{320}F_{24}N_{16}O_{40}P_{16}Pt_8S_8Zn_2$) *m/z*: [M-3OTf]$^{3+}$ 2,045.39, [M-4OTf]$^{4+}$ 1,497.38.

Synthesis and Characterization of 5d. Reaction scale was as follows: *cis*-Pt(PEt_3)$_2$(OTf)$_2$ (**1**) (7.44 mg, 10.20 mmol), potassium heptanedioate (1.21 mg, 5.12 mmol), Zn-**3** (1.74 mg, 2.55 mmol), and 2 mL of solvent. Compound **5d** was obtained as purple solid (7.7 mg, 91%). ^{1}H NMR (300 MHz, acetone-d_6): δ = 9.29 (m, 16H, α-Py-H), 9.15 (s, 8H, pyrrole-H), 8.65 (s, 8H, pyrrole-H), 8.52 (d, 16H, *J* = 5.4 Hz, β-Py-H,), 2.80 (br, 16H, CO_2CH_2), 2.26–2.10 (m, 96H, P-C*H*$_2$-CH$_3$), 1.66 (m, 24H, C*H*$_2$), 1.49–1.34 (m, 144H, P-CH$_2$-C*H*$_3$). ^{31}P{^{1}H}NMR (acetone-d_6, 121.4 MHz): δ = 7.68 (d, $^2J_{p\text{-}p}$ = 21.4 Hz, ^{195}Pt satellites, $^1J_{pt\text{-}p}$ = 3,248 Hz), 1.67 ($^2J_{p\text{-}p}$ = 21.4 Hz, ^{195}Pt satellites, $^1J_{pt\text{-}p}$ = 3,404 Hz). ESI-MS ($C_{212}H_{328}F_{24}N_{16}O_{40}P_{16}Pt_8S_8Zn_2$) *m/z*: [M-3OTf]$^{3+}$ 2,064.41, [M-4OTf]$^{4+}$ 1,511.42.

Synthesis and Characterization of 5e. Reaction scale was as follows: *cis*-Pt(PEt_3)$_2$(OTf)$_2$ (**1**) (6.18 mg, 8.47 mmol), potassium octanedioate (1.06 mg, 4.23 mmol), Zn-**3** (1.43 mg, 2.10 mmol), and 2 mL of solvent. Compound **5e** was obtained as purple solid (6.54 mg, 93%). ^{1}H NMR (300 MHz, acetone-d_6): δ = 9.27 (br, 16H, α-Py-H), 9.12 (s, 8H, pyrrole-H), 8.74 (s, 8H, pyrrole-H,), 8.54 (d, 16H, *J* = 5.4 Hz, β-Py-H), 2.80 (m, 16H, CO_2CH_2), 2.31–2.09 (m, 96H, P-C*H*$_2$-CH$_3$), 1.57 (m, 16H, C*H*$_2$), 1.48–1.33 (m, 144H, P-CH$_2$-C*H*$_3$), 1.23 (m, 16H, CH$_2$). ^{31}P{^{1}H}NMR (acetone-d_6, 121.4 MHz): δ = 7.37 (d, $^2J_{p\text{-}p}$ = 20.8 Hz, ^{195}Pt satellites, $^1J_{pt\text{-}p}$ = 3,253 Hz), 1.70 ($^2J_{p\text{-}p}$ = 20.8 Hz, ^{195}Pt satellites, $^1J_{pt\text{-}p}$ = 3,392 Hz). ESI-MS ($C_{216}H_{336}F_{24}N_{16}O_{40}P_{16}Pt_8S_8Zn_2$) *m/z*: [M-3OTf]$^{3+}$ 2,083.41, [M-4OTf]$^{4+}$ 1,525.43.

Spectroscopic Measurements. Absorption and fluorescence spectra were recorded on a Hitachi U-4100 and Hitachi F-7000 Spectrophotometer, respectively, with aerated spectroscopic-grade DCM, acetone, and DMSO (Sigma-Aldrich) at room temperature. The cells used in the experiments were 1-cm quartz cuvettes from Starna Cells. All samples were freshly prepared for each measurement. The extinction coefficients were determined by preparing four samples ranging in absorption from 0.01 to 1.0 with concentrations of 0.3–2.0 μM. The molar absorptivities for each solution were then calculated using Beer's Law, and the four were averaged. Subsequent samples were then prepared to confirm the extinction coefficients. The fluorescence quantum yield for **4** was calculated using rhodamine 6G standard (Φ = 0.88 in ethanol) (63), and the fluorescence quantum yield for **5** was calculated using rhodamine B (Φ = 0.50 in ethanol) (64).

ACKNOWLEDGMENTS. P.J.S. thanks the National Science Foundation (Grant NSF-CHE 0820955) for financial support. Y.S. and C.C. thank the National Natural Science Foundation of China (Grants 21071121 and 21172188) and the Priority Academic Program Development of Jiangsu Higher Education Institutions.

1. Cook TR, et al. (2010) Solar energy supply and storage for the legacy and nonlegacy worlds. *Chem Rev* 110(11):6474–6502.
2. Hagfeldt A, Boschloo G, Sun L, Kloo L, Pettersson H (2010) Dye-sensitized solar cells. *Chem Rev* 110(11):6595–6663.
3. Cracknell JA, Vincent KA, Armstrong FA (2008) Enzymes as working or inspirational electrocatalysts for fuel cells and electrolysis. *Chem Rev* 108(7):2439–2461.
4. Kim TW, Choi K-S (2014) Nanoporous $BiVO_4$ photoanodes with dual-layer oxygen evolution catalysts for solar water splitting. *Science* 343(6174):990–994.
5. Sivula K, Formal FL, Grätzel M (2009) WO_3–Fe_2O_3 photoanodes for water splitting: A host scaffold, guest absorber approach. *Chem Mater* 21(13):2862–2867.
6. Walter MG, et al. (2010) Solar water splitting cells. *Chem Rev* 110(11):6446–6473.
7. Prier CK, Rankic DA, MacMillan DWC (2013) Visible light photoredox catalysis with transition metal complexes: Applications in organic synthesis. *Chem Rev* 113(7): 5322–5363.
8. Liu Z, et al. (2004) Crystal structure of spinach major light-harvesting complex at 2.72 A resolution. *Nature* 428(6980):287–292.
9. Lokstein H, Härtel H, Hoffmann P, Woitke P, Renger G (1994) The role of light-harvesting complex II in excess excitation energy dissipation: An in-vivo fluorescence study on the origin of high-energy quenching. *J Photochem Photobiol B* 26(2):175–184.
10. Sauvage JP, et al. (1994) Ruthenium(II) and osmium(II) bis(terpyridine) complexes in covalently-linked multicomponent systems: Synthesis, electrochemical behavior, absorption spectra, and photochemical and photophysical properties. *Chem Rev* 94(4):993–1019.
11. Hoeben FJM, Jonkheijm P, Meijer EW, Schenning APHJ (2005) About supramolecular assemblies of π-conjugated systems. *Chem Rev* 105(4):1491–1546.
12. Webber SE (1990) Photon-harvesting polymers. *Chem Rev* 90(8):1469–1482.
13. Trenor SR, Shultz AR, Love BJ, Long TE (2004) Coumarins in polymers: From light harvesting to photo-cross-linkable tissue scaffolds. *Chem Rev* 104(6):3059–3077.
14. Hagfeldt A, Graetzel M (1995) Light-induced redox reactions in nanocrystalline systems. *Chem Rev* 95(1):49–68.
15. Sancar A (2003) Structure and function of DNA photolyase and cryptochrome blue-light photoreceptors. *Chem Rev* 103(6):2203–2237.
16. Lo S-C, Burn PL (2007) Development of dendrimers: Macromolecules for use in organic light-emitting diodes and solar cells. *Chem Rev* 107(4):1097–1116.
17. Li W-S, Aida T (2009) Dendrimer porphyrins and phthalocyanines. *Chem Rev* 109(11): 6047–6076.
18. Wasielewski MR (2009) Self-assembly strategies for integrating light harvesting and charge separation in artificial photosynthetic systems. *Acc Chem Res* 42(12):1910–1921.
19. Kim D, Osuka A (2004) Directly linked porphyrin arrays with tunable excitonic interactions. *Acc Chem Res* 37(10):735–745.
20. Iengo E, Zangrando E, Alessio E (2006) Synthetic strategies and structural aspects of metal-mediated multiporphyrin assemblies. *Acc Chem Res* 39(11):841–851.
21. Holten D, Bocian DF, Lindsey JS (2002) Probing electronic communication in covalently linked multiporphyrin arrays. A guide to the rational design of molecular photonic devices. *Acc Chem Res* 35(1):57–69.
22. Aratani N, Kim D, Osuka A (2009) Discrete cyclic porphyrin arrays as artificial light-harvesting antenna. *Acc Chem Res* 42(12):1922–1934.
23. Balaban TS (2005) Tailoring porphyrins and chlorins for self-assembly in biomimetic artificial antenna systems. *Acc Chem Res* 38(8):612–623.
24. Liang G, et al. (2006) Using enzymatic reactions to enhance the photodynamic therapy effect of porphyrin dityrosine phosphates. *Chem Commun (Camb)* (48):5021–5023.
25. Gu H, Xu K, Yang Z, Chang CK, Xu B (2005) Synthesis and cellular uptake of porphyrin decorated iron oxide nanoparticles-a potential candidate for bimodal anticancer therapy. *Chem Commun (Camb)* (34):4270–4272.
26. Huang Z (2005) A review of progress in clinical photodynamic therapy. *Technol Cancer Res Treat* 4(3):283–293.
27. Obata M, et al. (2009) In vitro heavy-atom effect of palladium(II) and platinum(II) complexes of pyrrolidine-fused chlorin in photodynamic therapy. *J Med Chem* 52(9): 2747–2753.
28. Allison RR, et al. (2004) Photosensitizers in clinical PDT. *Photodiagn Photodyn Ther* 1(1):27–42.
29. Sun RW-Y, Che C-M (2009) The anti-cancer properties of gold(III) compounds with dianionic porphyrin and tetradentate ligands. *Coord Chem Rev* 253(11-12):1682–1691.
30. Nam W (2007) High-valent iron(IV)-oxo complexes of heme and non-heme ligands in oxygenation reactions. *Acc Chem Res* 40(7):522–531.
31. Groves JT, Haushalter RC, Nakamura M, Nemo TE, Evans BJ (1981) High-valent iron-porphyrin complexes related to peroxidase and cytochrome P-450. *J Am Chem Soc* 103(10):2884–2886.
32. Tani F, Matsu-Ura M, Nakayama S, Naruta Y (2002) Synthetic models for the active site of cytochrome P450. *Coord Chem Rev* 226(1-2):219–226.
33. Meunier B (1992) Metalloporphyrins as versatile catalysts for oxidation reactions and oxidative DNA cleavage. *Chem Rev* 92(6):1411–1456.
34. Mansuy D (1993) Activation of alkanes: The biomimetic approach. *Coord Chem Rev* 125(1-2):129–141.
35. Dolphine D, Taylor TG, Xie LY (1997) Polyhaloporphyrins: Unusual ligands for metals and metal-catalyzed oxidations. *Acc Chem Res* 30(6):251–259.
36. Liu HY, Yam F, Xie YT, Li XY, Chang CK (2009) A bulky bis-pocket manganese(V)-oxo corrole complex: Observation of oxygen atom transfer between triply bonded Mn(V) [triple bond]O and alkene. *J Am Chem Soc* 131(36):12890–12891.
37. Gorin CF, Beh ES, Bui QM, Dick GR, Kanan MW (2013) Interfacial electric field effects on a carbene reaction catalyzed by Rh porphyrins. *J Am Chem Soc* 135(30):11257–11265.
38. Wielopolski M, et al. (2013) Blending through-space and through-bond π-π-coupling in [2,2′]-paracyclophane-oligophenylenevinylene molecular wires. *J Am Chem Soc* 135(28):10372–10381.
39. Ying X, et al. (2012) Second order nonlinear optical properties of corroles: Experimental and theoretical investigations. *J Porphyr Phthalocyanines* 16(12):1276–1284.
40. Wagner RW, Johnson TE, Lindsey JS (1996) Soluble synthetic multiporphyrin arrays. 1. Modular design and synthesis. *J Am Chem Soc* 118(45):11166–11180.
41. Prathapan S, Johnson TE, Lindsey JS (1993) Building-block synthesis of porphyrin light-harvesting arrays. *J Am Chem Soc* 115(16):7519–7520.
42. Wang JL, Wang C, Lin W (2012) Metal–organic frameworks for light harvesting and photocatalysis. *ACS Catalysis* 2(12):2630–2640.
43. Son H-J, et al. (2013) Light-harvesting and ultrafast energy migration in porphyrin-based metal-organic frameworks. *J Am Chem Soc* 135(2):862–869.
44. So MC, et al. (2013) Layer-by-layer fabrication of oriented porous thin films based on porphyrin-containing metal-organic frameworks. *J Am Chem Soc* 135(42):15698–15701.
45. Lee CY, et al. (2011) Light-harvesting metal-organic frameworks (MOFs): Efficient strut-to-strut energy transfer in bodipy and porphyrin-based MOFs. *J Am Chem Soc* 133(40):15858–15861.
46. Kent CA, et al. (2010) Energy transfer dynamics in metal-organic frameworks. *J Am Chem Soc* 132(37):12767–12769.
47. Kent CA, et al. (2011) Light harvesting in microscale metal-organic frameworks by energy migration and interfacial electron transfer quenching. *J Am Chem Soc* 133(33): 12940–12943.
48. Cook TR, Zheng YR, Stang PJ (2013) Metal-organic frameworks and self-assembled supramolecular coordination complexes: Comparing and contrasting the design, synthesis, and functionality of metal-organic materials. *Chem Rev* 113(1):734–777.
49. Chakrabarty R, Mukherjee PS, Stang PJ (2011) Supramolecular coordination: Self-assembly of finite two- and three-dimensional ensembles. *Chem Rev* 111(11):6810–6918.
50. Splan KE, Keefe MH, Massari AM, Walters KA, Hupp JT (2002) Synthesis, characterization, and preliminary intramolecular energy transfer studies of rigid, emissive, rhenium-linked porphyrin dimers. *Inorg Chem* 41(4):619–621.
51. Lee SJ, et al. (2008) Coordinative self-assembly and solution-phase X-ray structural characterization of cavity-tailored porphyrin boxes. *J Am Chem Soc* 130(3):836–838.
52. Kelley RF, et al. (2008) Intramolecular energy transfer within butadiyne-linked chlorophyll and porphyrin dimer-faced, self-assembled prisms. *J Am Chem Soc* 130(13): 4277–4284.
53. Dinolfo PH, Hupp JT (2001) Supramolecular coordination chemistry and functional microporous molecular materials. *Chem Mater* 13(10):3113–3125.
54. Wang M, Zheng Y-R, Ghosh K, Stang PJ (2010) Metallosupramolecular tetragonal prisms via multicomponent coordination-driven template-free self-assembly. *J Am Chem Soc* 132(18):6282–6283.
55. Wang M, Zheng Y-R, Cook TR, Stang PJ (2011) Construction of functionalized metallosupramolecular tetragonal prisms via multicomponent coordination-driven self-assembly. *Inorg Chem* 50(13):6107–6113.
56. Zheng Y-R, et al. (2010) A facile approach toward multicomponent supramolecular structures: Selective self-assembly via charge separation. *J Am Chem Soc* 132(47): 16873–16882.
57. Pollock JB, Cook TR, Schneider GL, Stang PJ (2013) Multi-component coordination-driven self-assembly: Construction of alkyl-based structures and molecular modelling. *Chem Asian J* 8(10):2423–2429.
58. Milanesil ME, et al. (2002) Synthesis and photophysical properties of Zn(II) porphyrin-C_{60} dyad with potential use in solar cells. *J Phys Org Chem* 15(12):844–851.
59. Spellane PJ, Gouterman M, Antipas A, Kim S, Liu YC (1980) Porphyrins. 40. Electronic spectra and four-orbital energies of free-base, zinc, copper, and palladium tetrakis (perfluorophenyl)porphyrins. *Inorg Chem* 19(2):386–301.
60. Even U, Magen J, Jortner J, Friedman J, Levanon H (1982) Isolated ultracold porphyrins in supersonic expansions. I. Free-base tetraphenylporphyrin and zinc-tetraphenylporphyrin. *J Chem Phys* 77(9):4374–4383.
61. Makarska M, Radzki St, Legendziewicz J (2002) Spectroscopic characterization of the water-soluble cationic porphyrins and their complexes with Cu(II) in various solvents. *J Alloys Compd* 341(1-2):233–238.
62. Ghirotti M, et al. (2007) Energy transfer pathways in pyridylporphyrin Re(I) adducts. *Inorg Chim Acta* 360(3):1121–1130.
63. Fischer M, Georges J (1996) Fluorescence quantum yield of rhodamine 6G in ethanol as a function of concentration using thermal lens spectrometry. *Chem Phys Lett* 260(1-2): 115–118.
64. Karstens T, Kobs K (1980) Rhodamine B and rhodamine 101 as reference substances for fluorescence quantum yield measurements. *J Phys Chem* 84(14):1871–1872.